ADVANCED FUNCTIONAL MATERIALS
www.afm-journal.de

Spider-Inspired, Fully 3D-Printed Micro-Hydraulics for Tiny, Soft Robotics

Gabriel L. Smith, Joshua B. Tyler, Nathan Lazarus, Harvey Tsang, Luis Viornery, Jeffrey Shultz, and Sarah Bergbreiter**

Many arachnids use internal hemolymph pressure to actuate extension in their leg joints. The inherent large foot displacement-to-body length ratio that arachnids can achieve through hydraulics relative to muscle-based actuators is both energy and volumetrically efficient. Until recent advances in nano/microscale 3D printing with two-photon polymerization (2PP), the physical realization of synthetic complex 'soft' joints would have been impossible to replicate and fill with a hydraulic fluid into a sealed sub-millimeter system. Inspired by nature, the smallest scale 3D-printed hydraulic actuator (4.9×10^{-4} mm^3) by more than an order of magnitude is demonstrated. The use of stiff 2PP polymers with micron-scale dimensions enable compliant membranes similar to exoskeletons seen in nature without the requirement for low-modulus materials. The bio-inspired system is designed to mimic similar hydraulic pressure-activated mechanisms in arachnid joints utilized for large displacement motions relative to body length. Using variations on this actuator design, the ability to transmit forces with relatively large magnitudes (milliNewtons) in 3D space is demonstrated, as well as the ability to direct motion that is useful towards microrobotics and medical applications. Microscale hydraulic actuation provides a promising approach toward the transmission of large forces and 3D motions at small scales, previously unattainable in wafer-level 2D microelecromechanical systems (MEMS).

1. Introduction

Soft robotics can provide large deformations and high degrees of freedom that enable them to interact with unstructured environments.[1] While most of the research in soft robotics has focused on larger scale systems (from centimeters to meters), these benefits can also be realized at small (millimeter and sub-millimeter) scales. A variety of tiny organisms take advantage of soft, flexible, compliant structures for locomotion, including insect larvae[2] and worms.[3] Insect larvae have even demonstrated high performance jumps more frequently associated with rigid systems.[4] Robotic systems with similar soft and compliant properties hold great promise for medical use[5–11] and can be further useful for biomedical applications if smaller features (e.g., sub-100 µm) can be achieved.[12]

These promising applications have inspired a wide variety of methods for fabricating soft robotics including molding and 3D printing[1] that take advantage of soft, low-modulus materials to achieve compliant structures. However, fabrication processes that integrate low-modulus materials in sub-millimeter mechanisms are much less common.[13–15] These processes are often limited to two dimensional molding and casting in contrast to the 3D shapes at larger scales.

Soft actuation at small scales can be even more challenging. At large scales, pneumatics are a common transduction approach,[16] but pneumatics are particularly challenging to scale down to sub-millimeter scales due to the challenge of interfacing and sealing the air supply to the soft structure.[15,17,18] A variety of other soft actuators have been used in the literature including electrostatic,[19] thermal and shape memory alloy,[20–22] and hydraulic.[17,23–25] While a number of small, soft actuators and compliant microgrippers have been previously demonstrated, including some that use 3D printing (e.g., [13, 26–31]), soft actuation has not been integrated with soft robot structures at sub-millimeter scales.

In this work, we take inspiration from the hydraulically-driven, compliant structure of small arachnids like spiders and mites that enable incredibly high displacement-to-body length

G. L. Smith, J. B. Tyler, N. Lazarus, H. Tsang
US Army Research Laboratory
Adelphi, MD 21043, USA
E-mail: gabriel.l.smith12.civ@army.mil
N. Lazarus
Department of Electrical and Computer Engineering
University of Delaware
Newark, DE 19716, USA
L. Viornery, S. Bergbreiter
Department of Mechanical Engineering
Carnegie Mellon University
Pittsburgh, PA 15213, USA
E-mail: sbergbre@andrew.cmu.edu
J. Shultz
Department of Entomology
University of Maryland
College Park, MD 20742, USA

The ORCID identification number(s) for the author(s) of this article can be found under https://doi.org/10.1002/adfm.202207435.

DOI: 10.1002/adfm.202207435

ratios.[32] In arachnids, the leg joints are configured in a way such that muscle-driven extension is not possible.[33–35] While active muscles traversing these joints induce leg flexion, leg extension is instead induced by hydraulic pressure generated within the prosoma (the head and thorax of the spider).[32,33,36] This centrally located pressure in the prosoma induces a flow of hemolymph (the spider's hydraulic fluid) from the prosoma into the legs. Similarly, this work uses a central pressure source to induce flow to multiple microactuators.

Spiders have already inspired numerous other engineered hydraulic actuation approaches, although these are typically demonstrated at scales that are orders of magnitude larger than the spider.[37–39] A centimeter-scale spider-inspired joint powered by electrohydraulic actuators and using soft materials was demonstrated in [37], and a similar centimeter-scale system using electro-conjugate fluids and microfabricated pumps was shown in [39]. The centimeter-scale spider-inspired hydraulic joint in [38] was used to power jumps, similar to a jumping spider. This work was particularly interesting because it also mimicked the complex folding mechanism of the spider's cuticular membrane using 3D printing, albeit with a relatively low modulus (40 MPa) material. Spiders have even been used as an entire robotic gripping system with the recent example of "necrobotics".[40] Engineered versions of spider-inspired hydraulic actuation offer numerous advantages however, primarily driven by the ability to design more arbitrary structures that can be adapted to specific applications. The scaling analysis in [40] also highlights robotic grippers even smaller in size as targeted in this work should benefit from higher grip forces normalized to the weight of the gripper.

In this work, our goal was to demonstrate multi-functional (stiff, compliant, and fluidic) properties with a single material at micron-scale, spider-like thicknesses using commercially available resins with a chitin-like modulus. Similar to the structural design inspiration used in [38], we also took inspiration from the spider's exoskeleton that maintains compliance in the leg joints through structural design.[41] Although it is compliant, a spider's leg joint consists of chitin-protein cuticle, a relatively high modulus material, throughout the joint indicating the possibility of "soft" behavior with higher modulus materials. At the microscale, these materials become compliant enough to be useful in soft robotics due to nonlinear scaling of flexural rigidity with thickness.

As such, the primary contribution of this work is a demonstration of hydraulic actuation using a fully 3D printed micron-scale exoskeleton made from a high modulus material. Similar to arachnids, the microscale hydraulic actuators in this work can displace on the order of approximately one body length. While the design is only one element toward replicating spider ambulation, this work represents a significant step toward achieving large forces and displacements in multiple remote actuators from a single pressure source with commercially available resins. We also demonstrate for the first time a novel approach to filling a 3D printed microscale hydraulic system. We use the uncured photoresist to eliminate the need to fill such a tiny microstructure. While larger, centimeter-scale spider-inspired hydraulic actuators (e.g., [37–39]) can use syringes to add hydraulic fluid, filling and sealing a pressurized system at this scale would also present incredible challenges. The in-situ filling approach demonstrated in this work sidesteps this challenge.

2. Results and Discussion

2.1. Imaging Lycosid Exoskeletons

As mentioned previously, a spider induces leg extension by generating pressure within the prosoma.[32,33,36] This pressure induces a hemolymph flow into the legs that is transmitted from the prosoma to the respective joints via lacunae, which are hemolymph-filled spaces between all soft tissues inside a leg. The increased volume of these joints results in leg extension.[32] The pressures generated can be quite high. For instance, in *Eratigena atrica*, one arachnid species, internal pressures were measured up to 50 kPa.[33]

To better understand how the lacunae (the empty space for hydraulic fluid behind the exoskeleton) and exoskeleton geometry of a spider enable this actuation, we used micro computed tomography (micro-CT, ZEISS Xradia 510 Versa) to scan the leg of a *Rabidosa rabida* specimen from the family Lycosidae (micro-CT video in Supporting Information). The lycosid is commonly referred to as the wolf spider and is depicted in **Figure 1**a. The lycosid leg joint in Figure 1b is several hundred micrometers in diameter, and the cross-section of this joint imaged in Figure 1c is particularly interesting. The thickness of the outer portion of the exoskeleton at the joint was measured at 15–20 μm while the thickness of the inner flexible region of the joint varied from approximately 1–5 μm.

The spider cuticle found in these joints is an anisotropic and hierarchical composite. Its elastic properties depend upon the volume fraction of chitin and various proteins, and can vary widely based on fiber orientation and hydration. Pure chitin fibers are predicted to be around 100 GPa along the long axis, but the protein-chitin composite cuticle has been measured across a wide range of 0.1–20 GPa.[41,51] Despite this relatively high modulus material, the small thickness of the spider's joint membrane enables it to behave as a compliant flexible mechanism, thereby enabling a wide range of motion. To better illustrate this design space of thickness and material modulus, we have calculated a heat map of flexural rigidity for a simple cantilever beam in Figure 1d. Flexural rigidity is used as a proxy for compliance in this case, and is the product of the material's Young's modulus, E, and moment of inertia, I. In the case of a thin beam, the moment on inertia is,

$$I = (1/12)b * t^3 \quad (1)$$

where b is the beam width and t is the beam thickness. Note the cubic relationship of I to t; the flexural rigidity scales down rapidly as thickness is reduced. As such, a high modulus material can behave compliantly when reduced to very small thicknesses on the order of microns. As seen in Figure 1d, a modulus choice of 1–10 GPa, similar to chitin, can achieve similar flexural rigidity to previous work in soft robotics when printed with feature sizes ranging from 1 to 100 μm. Even higher modulus materials can be used to create the compliant mechanisms

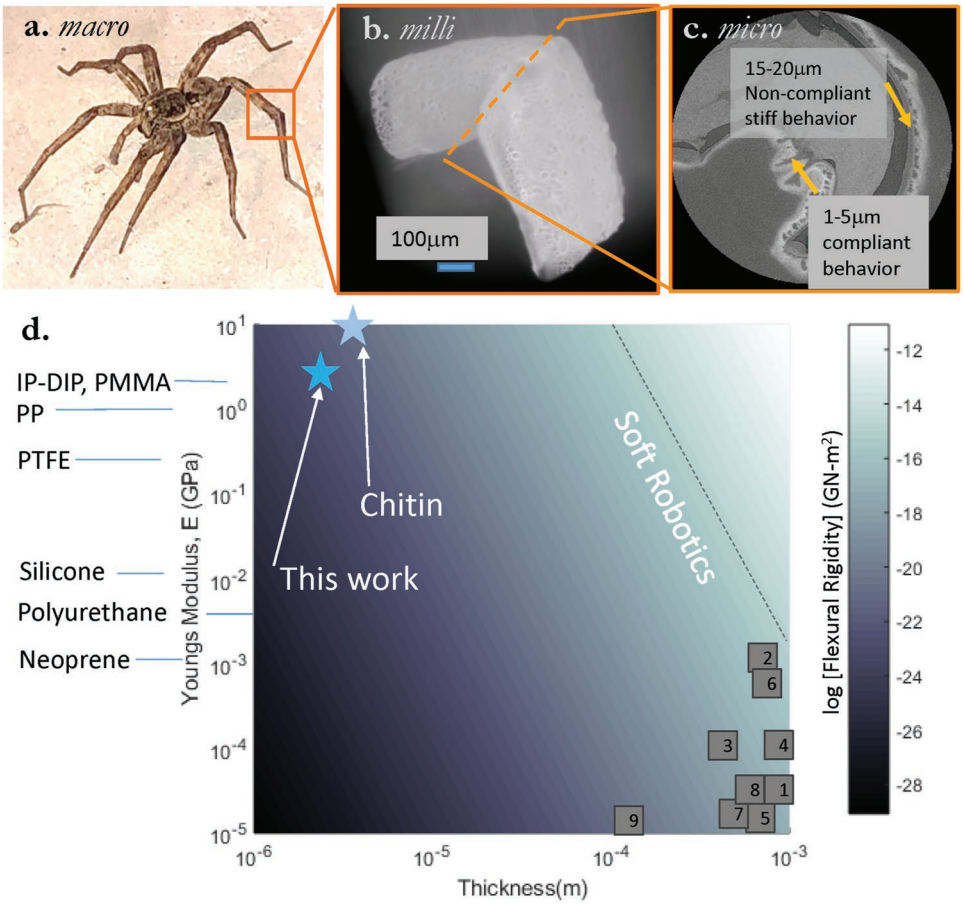

Figure 1. Enabling 'soft' systems with small feature sizes. a) An example of a wolf spider from the family Lycosidae, b) CT scan of a Lycosidae *Rabidosa rabida* front leg, c) cross section showing compliant and non-compliant regions, d) colormap highlighting how chitin (and IP-DIP used in this work) can be thought of as compliant materials for soft robotics at small feature sizes. The figure shows how flexural rigidity of a cantilever made with the given material properties and thicknesses changes over this parameter space. Low flexural rigidity can be useful in numerous soft robotic systems and these results highlight the similarity of the parameters used in this work to naturally found hydraulic systems made from hard chitin. Several additional references from 3D-printed elastomeric soft materials commonly found in the soft robotics community are also provided. Data points 1–9, respectively, are from [42–50]. (IP-DIP: Nanoscribe resin used in this work, PMMA: poly[methyl mthacrylate], PP: polypropylene, PTFE: polytetrafluoroethylene.)

needed for soft robotic systems if they become available for manufacture at even smaller scales.

In the spider micro-CT scans, a high-modulus material like cuticle can behave as both a more rigid structure in the leg segments as well as a more compliant structure in the joints, just by changing the thickness of the material. We replicated this thickness variation in our test structures and used dimensions similar to those observed in the micro-CT scans. The advantage of this design approach is the ability to achieve load carrying and compliance in a 3D printed structure made from a single material. The extreme compliance demonstrated in this work is due to the very thin walls that can be fabricated.

2.2. Fabrication of Spider-Inspired Hydraulic Microactuators

Though wafer-level MEMS processing has been able to fabricate layered 2D micro hydraulic structures for decades,[52] it was not until recent advancements in additive manufacturing (AM) that fabricating 3D synthetic complex structures, like those we see in nature at the microscale, has become possible. The fabrication process shown in **Figure 2**a–c uses two-photon polymerization (2PP) on a Nanoscribe Photonic Professional 3D printer to print the test structures and soft robotic systems in this work (e.g., Figure 2d). The IP-DIP resin used in this process is commercially available from Nanoscribe and has an estimated Young's modulus of approximately 2.1GPa. While a lower modulus resin (IP-PDMS, E ≈ 15.3 MPa) has recently become available from Nanoscribe, very little work has successfully shown its use in printing complex 3D structures.[53] Fabricated microactuators were developed in propylene glycol monomethyl ether acetate (PGMEA) followed by isopropanol, and allowed to air dry.

A bellows test structure is printed with a designed wall thickness of 1 μm to provide system compliance similar to that found on the inner membrane of the spider leg. Rigid parts of the test structure in Figures 2d–f are printed with wall thicknesses of 5–10 μm. While many hydraulic bellows-type actuators use soft materials[1,37,39] to reduce stiffness, the 1 μm thick bellows' sidewalls effectively reduce the relative mechanical stiffness of the

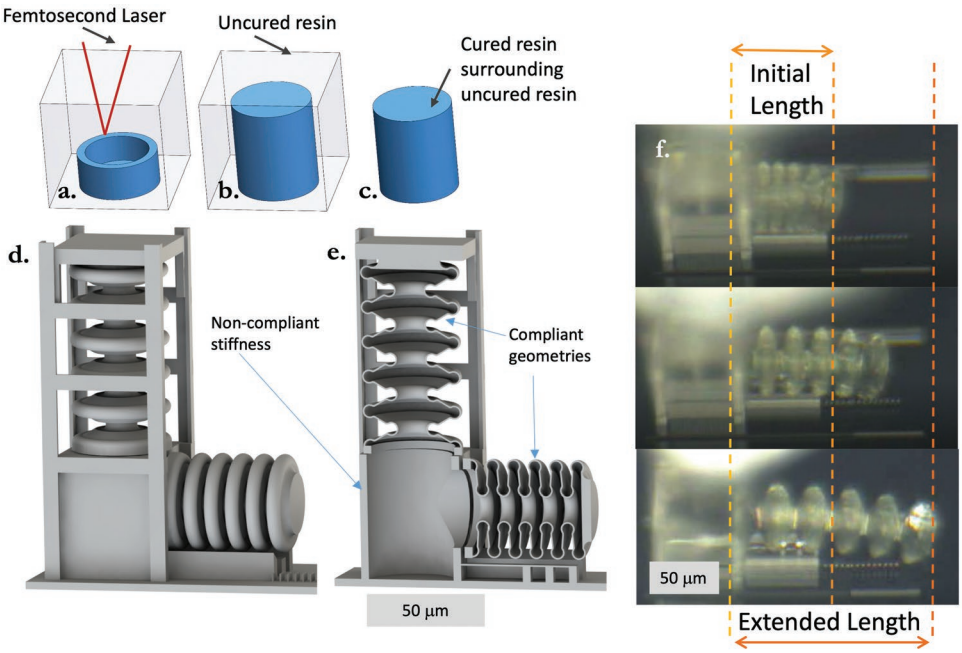

Figure 2. Schematics and images of the fabrication process and linear extension microactuator design. a) Two converging beams in 2PP curing within a drop of IP-DIP resin, b) a closed volume of resin with liquid resin inside and outside of the cylinder, c) the same closed volume with the external resin removed, d) a linear extension microactuator with bellows at the input and output of the device, e) a cross-section of the same structure, and f) progressive testing of the same feature, noting the 1:1 displacement-to-actuator length ratio.

structure despite the relatively high material modulus as indicated in Figure 1d.

As shown in Figure 2a–c, a novel contribution to this printing process is the encapsulation of uncured resin as the hydraulic fluid. Adding hydraulic fluid into an actuator this small is a challenge for two key reasons. The smallest syringe tips (e.g., a 34 gauge needle) have an outer diameter larger than the printed bellows structure. In addition, to fill a printed microscale bellows structure with a hydraulic fluid, it would be necessary to first remove the uncured resin from the structure and reseal it without adding any air to the actuator—both of which are challenging fabrication tasks. More typically in 2PP printing, closed volumes of uncured resin are avoided and unexposed resin is removed from the print using solvents in the developing process. By encapsulating a volume of resin, the developer (PGMEA) cannot reach the enclosed resin, leaving it to serve as a hydraulic pressure transfer medium inside the intentionally designed compliant structures. The resulting hydraulic structures are also free from any compressible gas like air, making them more efficient at transferring force within the system.

In addition, print times for these relatively large structures (heights and lengths of ≈ 200 µm) printed at the Nanoscribe's highest resolution using its 63× objective lens are typically hours to days if the laser must cure every interior voxel. For the demonstrated actuators, the Nanoscribe laser only needed to cure a layer on the order of 1 µm thick for the sidewalls. This process resulted in print times that were typically less than 1h.

Device yield from the fabrication process was very good overall. During the design process for these microscale hydraulic actuators, several failures occurred (e.g., bursting, leaking), resulting in design and fabrication iterations. Tuning printing power levels to achieve a continuous membrane and choosing a nominal minimum wall thickness of 1 µm were the most important parameters to achieve the functional design. Once the design and process were validated, the yield was 100% with over 20 actuators printed. Occasionally over the course of this work, yield dropped when 2PP parameters out of our control were modified. For instance, a new laser source was installed on the Nanoscribe during the course of this study. Print parameters, including laser power, needed to be slightly adjusted to return to a high yield process. Extensive quantification of 2PP and Nanoscribe parameter effects are available in the literature[54,55] and outside the scope of this paper.

2.3. Hydraulic Linear Extension Microactuator Design

The first actuator designed was a 90° linear extension actuator shown in Figure 2d–f. The 90° extension design demonstrates the concept of transferring a force applied to a vertically oriented input bellows to a horizontally oriented output bellows. In operation, the fluid pressure generated by pushing down on the input expanded the output bellows (Figure 2f). In the 90° design, a round bellows input was connected with a round bellows output through a 90° joint. A platform and guide were integrated around the actuator to reduce the input bellows' degrees of freedom for ease of characterization.

Both input and output bellows were designed with a 50 µm diameter and a nominal sidewall thickness of 1 µm. This sidewall thickness was varied from 0.8 to 1.2 µm for both modeling and print testing. In early fabricated designs, the 1 µm sidewall printed the most consistently, was sufficiently compliant, and

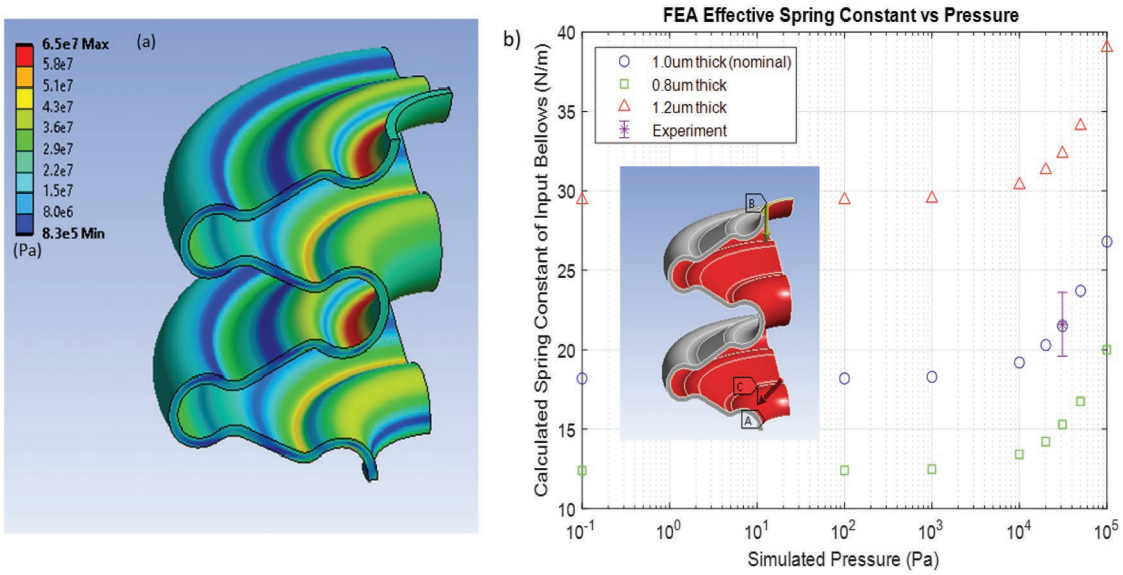

Figure 3. a) ANSYS FEA results showing von Mises stress in Pascals after a simulated 10 µm displacement and internal ramping pressure. The applied boundary conditions are shown in the inset in Figure 3b–A: fixed displacement , B: 10 µm axial displacement, and C: internal pressure. The cyclic periodic axisymmetric condition was applied to the planar faces. b) The effective spring constant was calculated for a range of applied internal pressures with three different sidewall thicknesses: 0.8, 1.0, and 1.2 µm. Experimental data is shown with the purple point at 31 kPa indicating the approximate expected pressure generated by the fabricated input bellows.

able to withstand the applied pressure. The 0.8 µm designs were less reliable and often burst upon test force application. The 1.2 µm designs were stiffer than was ideal for the measurement setup. Thicker designs could be explored further if larger force actuators were needed in the system.

The input was designed as an expanded bellows and the output was designed as an initially collapsed bellows. The bellows input to output diameter ratio was 1:1. In future designs, the input:output bellows diameter ratio can be modified to realize an increase in output displacement or force from lower input displacement or force, respectively. Thicker walls were used in the base structure that connects the input bellows and the output bellows to constrain the fluid directing the internal pressure created from pushing down on the input bellows. This is similar to the thicker cuticle structures in the spider joint used to provide rigidity.

ANSYS Workbench (2022 R2) finite element models were used to guide design iterations and also predict performance of the printed actuators. To balance computation time and model accuracy, a reduced cyclic-region axisymmetric model of the 3D bellows was developed to better capture bending and stress in the bellows' sidewalls (**Figure 3**a). To simulate the hydraulic loading that will result when compressing the bellows, a variable maximum pressure from 0 to 100 kPa was applied to the elements of the bellows' interior to represent the fluid pressure on the sidewalls of the bellows actuator. This pressure was increased linearly with displacement to simulate the output bellows increasing strain energy and reaction pressure back into the fluid. The bellows' base was placed under a fixed support boundary condition while a 10 µm displacement was applied to the top of the bellows segment (Figure 3b inset). The model was densely meshed with four elements through the thickness resulting in over 1.2 million nodes.

This ANSYS model was primarily used to explore the effect of sidewall thickness and internal fluid pressure on the input bellows' stiffness, as well as the resulting stresses that occur with applied deformations. As shown in Figure 3b, the effective stiffness of the bellows increases with applied hydraulic pressure. This pressure is important because the fluid pressure will ultimately be used to drive the output bellows and must overcome the intrinsic stiffness in these output bellows to do useful work. The effect of the bellows' sidewall stiffness (0.8, 1.0, and 1.2 µm) was also varied in this analysis. It is clear from Figure 3b that the sidewall thickness has a significant effect on the bellows' stiffness as expected; a small increase from 1.0 to 1.2 µm results in a nominal stiffness increase over 50% (at negligible hydraulic pressure). While this complex 3D bellows design is not as simple as the flexural rigidity used to illustrate the effect of sidewall thickness in Figure 1d, this nonlinear trend in compliance is clearly still present in the finite element results.

The ANSYS model also highlights regions of high equivalent stress in Figure 3b. The simulated 10 µm displacement resulted in a maximum von Mises stress of 65 MPa for the 1 µm wall thickness design as shown in Figure 3a. This maximum stress value is near the reported yield stress of this material, 67.2 +/− 4.7 MPa, found in the literature.[56] As a result, some plastic deformation may be expected if applied displacements increase beyond this range. Future bellows designs could also modify these regions to reduce stress. Aside from being initially compressed, the output bellows structure was designed with the same geometry, shown in Figure 2e, and therefore was expected to have the same spring constant and stress.

2.4. Hydraulic Linear Extension Microactuator Testing

The hydraulic microactuators were primarily characterized on their force-displacement performance and how this

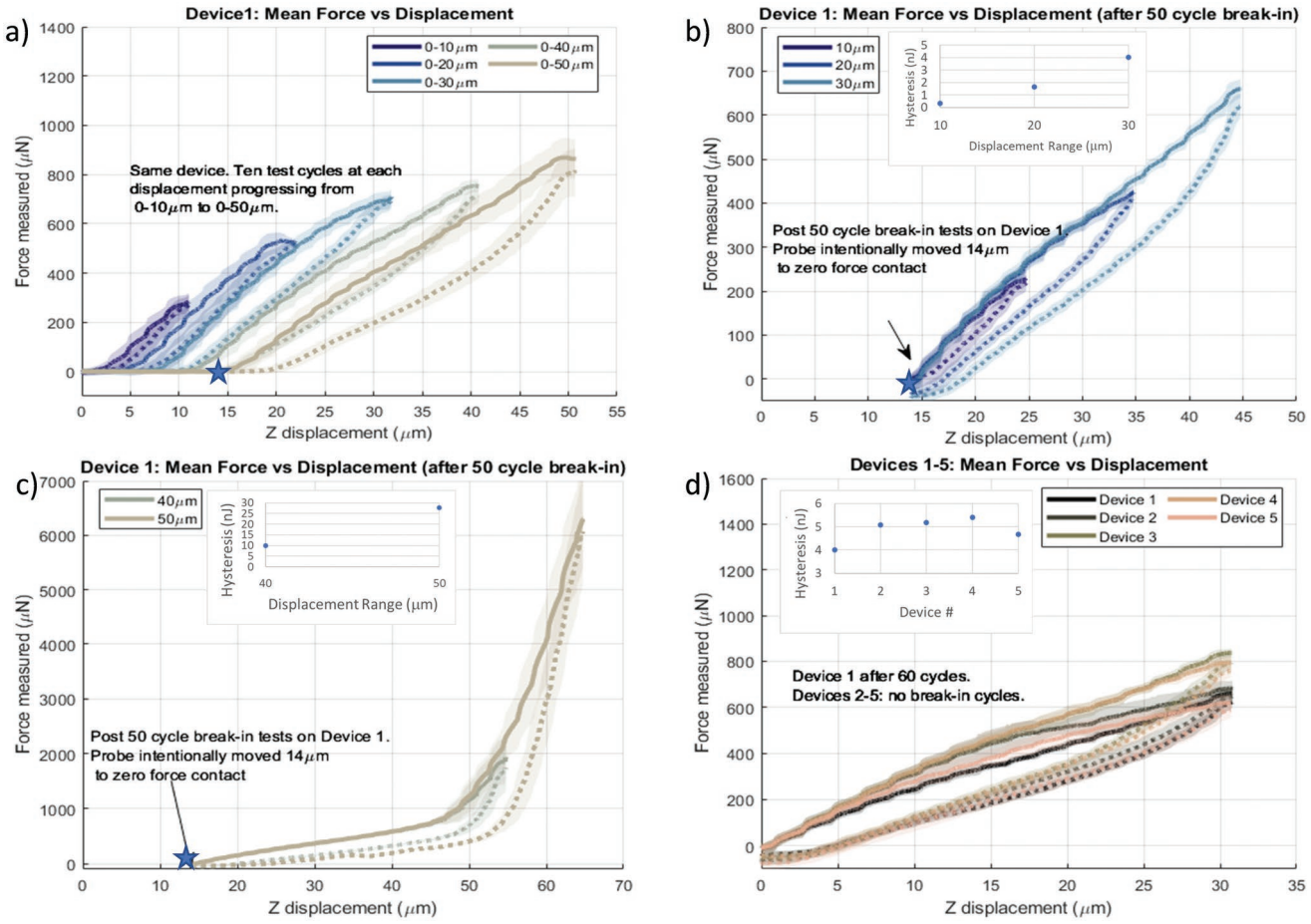

Figure 4. Results from force-displacement experiments on the linear extension actuator. In all plots, the mean and standard deviation are plotted with lines and shading respectively. Increasing applied displacements are marked with a solid line while decreasing applied displacements are noted with a dotted line. a) 10 cycles each of five different input displacements (10, 20, 30, 40, and 50 μm) are applied. b) After the 50 cycles applied in (a), the force sensor probe is adjusted to the new zero force condition marked with a star after the actuator plastically deforms. 5 cycles each of three different input displacements (10, 20, and 30 μm) are applied from this new zero position showing consistent behavior. c) 5 further cycles each of two different input displacements (40 and 50 μm) are applied from the new '0' position showing both consistent behavior but also increased stiffness at larger displacements as the bellows sidewalls come into contact. d) The 30 μm displacements in (b) are compared to 5 cycles each of 30 μm displacements measured from three more printed actuators (Devices 2–4) and 4 cycles of 30 μm displacements measured from one more printed actuator (Device 5). The zero position of Devices 2-5 was reset after each cycle. Insets in (b–d) indicate calculated energy loss from the relevant mean actuation cycle.

performance changed over actuation cycles and across devices. In this case, forces on the input bellows were measured along with the displacement of the input bellows, effectively measuring the stiffness of the microactuator. Input forces and displacements were quantified with a Femtotools FT-S1000 probe and the Femtotools control system. Knowledge of this stiffness is critical for future designs that may utilize an electrically driven actuator to deform the input bellows. In addition, the IP-DIP resin is relatively viscous for a hydraulic fluid (≈2420 mPa s[57]) and as such, it is important to understand various losses in the hydraulic actuation system. Finally, the output displacement was quantified optically with a Keyence VHX-1000 digital microscope with a 2 μm uncertainty at 500x magnification.

Data from force-displacement experiments is shown in **Figure 4**. Input *z*-displacement is shown on the *x*-axis: a 0 μm displacement indicates a fully expanded input bellows and a 50 μm displacement indicates a collapsed input bellows. At the maximum tested input displacement of 74 μm (not shown in this figure), the input bellows is fully collapsed and the output bellows is expanded as shown in Figure 2f. The applied force as measured by the FemtoTools probe is indicated on the *y*-axis with an estimated uncertainty of 10 μN.

To explore how stiffness and energy lost in the actuator changes over cycles and displacements, 10 actuation cycles each were applied to the actuator starting with 10 μm displacements and increasing to 50 μm displacement inputs in increments of 10 μm. This resulted in 50 total cycles applied to the actuator. The mean (line) and standard deviation (shading) of these results are provided in Figure 4a. All 50 cycles were started from the same 0 position as referenced from the FemtoTools probe. However, it is clear that the displacement at which the probe starts applying force to the bellows increases as more cycles are applied to the actuator. We hypothesize that this is due primarily to plastic deformation in the printed bellows but also due to 'unsticking' observed under the microscope in the

output bellows over the first several cycles. This unsticking behavior can be observed in the first 6 s of Video S2 (Supporting Information) and the first cycle plot in Figure S1b (Supporting Information).

This hypothesis is supported by the data in Figures 4b,c. Figure 4b shows data from 15 more cycles (5 cycles each of 10, 20, and 30 μm displacements) applied to the actuator after the original 50 cycles in Figure 4a. The star represents the new zero position (14 μm) captured after the final cycle in the previous plot. In this dataset, the starting position no longer changes after each cycle. Similarly, Figure 4c shows data from a further 10 cycles (5 cycles each of 40 and 50 μm displacements). The starting position no longer changes over these cycles either. This data indicates that the actuator has relatively consistent behavior after some number of 'break-in' cycles (in this case, the 50 cycles applied in Figure 4a).

There are several other notable features of the device performance found in these two figures including repeatability and changes in stiffness. As can be seen in Figure 4b, the mean standard deviation across all of these cycles is small (22.6, 18.1, and 18.6 μN across the loading curves for 10, 20, and 30 μm respectively) and close to the uncertainty of the force sensor, 10 μN. The larger standard deviation seen in Figure 4a is due largely to the break-in process. In addition, the stiffness calculated from the slope of the loading curves (solid line) is consistent across all 15 cycles with 21.3, 20.4, and 21.5 N m^{-1} for 10, 20, and 30 μm displacements, respectively. However, in Figure 4c, the stiffness increases dramatically at larger applied displacements of 40 and 50 μm from the new starting position due to contact between the bellows sidewalls. This increase was not observed in Figure 4a because the maximum displacements from the 'true' zero position were < 40 μm.

In addition, the hysteresis and resulting energy lost during an actuation cycle increases as the displacement increases. When redirecting forces via hydraulic fluid, we also expect a reduction in energy at the output due to the strain energy stored in the bellows material. Ideally, the majority of this energy can be utilized to return the actuator to its original position, with minor losses due to viscoelastic and fluidic losses, but high viscosity at small scales is a concern. Detailed quantification of these various losses is outside the intended scope of this paper but the total loss is evidenced in the force-displacement curves of Figure 4. From this data, the energy lost at a 10 μm displacement is found to be 0.31 nJ, which is approximately 24% of the mean maximum input energy of 1.3 nJ. In contrast, the energy lost over a 30 μm displacement is approximately 4.0 nJ that represents 38% of the maximum input energy of 10.6 nJ. Clearly this energy loss would not be ideal for high frequency actuators, but is not unreasonable for anticipated low duty cycles for this type of robotic soft actuator. Moreover this could be reduced if a less viscous hydraulic fluid could be realized.

To evaluate variation across multiple printed actuators, four additional actuators were printed concurrently with identical print parameters and were compared to the first device characterized in Figures 4a–c. Figure 4d shows the force-displacement measurements of all five actuators with applied displacements of 30 μm. While there were no break-in cycles applied to devices 2–5, device 1 is plotted with the same data found in Figure 4b after 60 break-in cycles. The data is relatively consistent across devices, but it is interesting to note that devices 2–5 show a slightly larger stiffness. This larger slope in force-displacement is consistent in devices 3 and 4 and reduces at larger displacements in devices 2 and 5. These results are consistent with the previous observation that the output bellows can stick to itself during the first several cycles resulting in higher observed stiffness in early cycles.

Though direct internal pressure would be challenging to measure in this setup, by combining the finite element simulation and experimental data we can infer the magnitude of the hydraulic pressure in the system. The value of this pressure was calculated from a second order fit of simulated results (1 μm sidewall thickness) in Figure 3b. The average slope of the 0 – 30 μm curve in Figure 4b is calculated at 21.5 N m^{-1}. This is represented with the purple marker in Figure 3b and corresponds to an estimated fluid pressure of 31 kPa. Running the ANSYS model with this calculated internal pressure matches the experimental force required to displace the bellows 30 μm. This estimated pressure is similar in magnitude to the aforementioned pressures measured in *Eratigena atrica* spider legs of 50 kPa for comparison.[33] These results indicate that the model is a good representation of the fabricated micro-hydraulic actuator.

Output measurements taken from a video of the horizontally oriented output bellows were quantified utilizing the proprietary system software packaged with the Keyence digital microscope. This output displacement is shown progressively in Figure 2f. The maximum output displacement measured for this design ((Extended length) - (Initial length) in Figure 2f) was 73 ± 2 μm. This displacement represents >100% of the bellows' 70 μm initial length demonstrating that actuator relative displacement is on the order of one body length.

Finally, given the use of the photosensitive resin as the hydraulic fluid, we also tested how the actuator would perform over time when exposed to typical laboratory lighting conditions. Previous experiments showed that exposure to 390 nm UV light for < 30 min was enough to fully cure the actuator thereby negating its functionality. Force-displacement data was captured for a separately printed actuator exposed to both fluorescent and incandescent lighting (measured light spectrum and force-displacement data can be found in Supporting Information). The incandescent source was chosen for its broad, relatively uniform, range of optical wavelengths. Not surprisingly, given the minimal exposure to the 390nm light needed to cure the photoresist, very little change was observed in force-displacement data measured immediately after printing, and after 2, 4, and 6 days of light exposure. Based on this data, the internal resin appears to undergo insignificant change after prolonged exposure to laboratory lighting.

2.5. Hydraulic Lateral Bending Microactuator Design and Testing

In addition to the extension actuator design described above, lateral actuators were also designed for testing. These lateral actuators (**Figure 5**a–c) constrain one side of the output bellows resulting in lateral bending when internal fluid pressure is applied through compression of the input bellows. This is a very similar design to many soft actuators in the literature.[58,59]

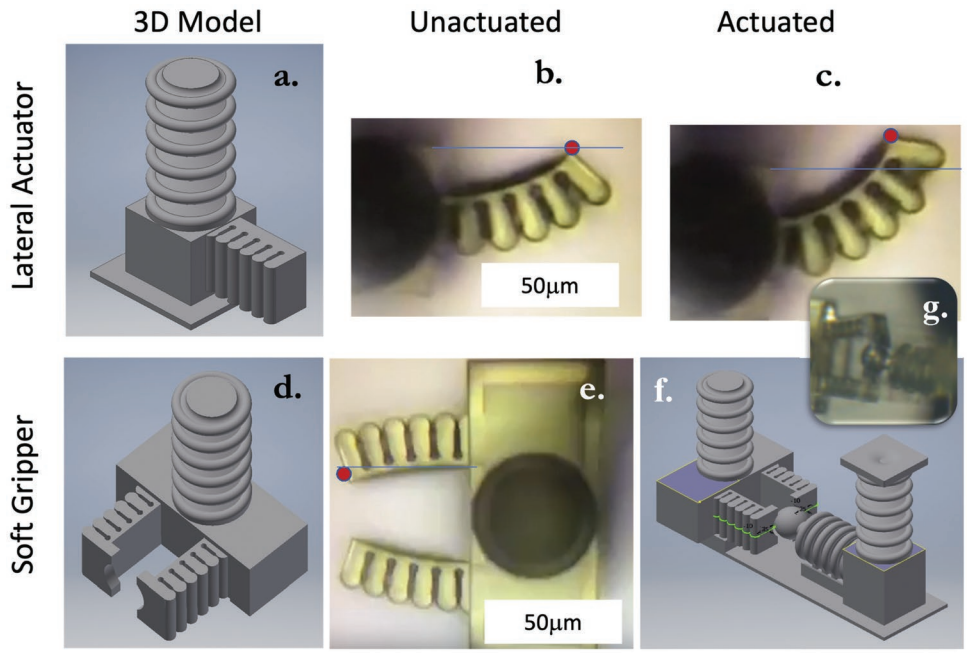

Figure 5. Design and results from the lateral bending microactuator and soft microgrippers. a) a 3D model of the lateral microactuator, b) top-down view of the lateral microactuator as printed, c) top-down view of the lateral microactuator when actuated on a probe station, d) 3D model of the opposing lateral microactuators in a gripper configuration, e) a top-down view of the normally open soft microgripper as printed, f) the normally open microgripper model and g) the same design gripping a sphere positioned by a linear extension actuator on a probe station.

The input bellows was the same design as that used in the extensional actuator design.

Similar to the extension actuator, the resin shell thickness was printed with a designed wall thickness of 1 μm and thicker walls were used in the base structure that connects the input bellows and the lateral actuator. As the individual sections expand they push against one another resulting in a asymmetric expansion on one side (Figure 5b,c). It should be noted that the printed lateral actuator (Figure 5b) curves after printing and is not straight as designed (Figure 5a) due to non-uniform polymer shrinkage as the polymer cures and develops. Once quantified for this geometry, this effect could be easily compensated for in the initial design with a reverse curvature.

The lateral actuators were also designed with a 50 μm diameter input bellows and when actuated with a 50 μm input displacement, the lateral actuator tip (indicated by the red dot in Figure 5b,c) displaced a total of 33 μm from its released deflection. Force-displacement curves were not measured for this actuator, but similar issues with sticking between the expansive portion of the output bellows were observed. Successful demonstration of the lateral design was achieved in the first iteration based on lessons learned while designing and printing the linear extension actuators.

2.6. Soft Robotic Microgrippers

Two separate soft robotic microgrippers were fabricated using combinations of lateral actuators and linear extension actuators. The first design used two lateral actuators operating in opposite directions (Figure 5d–f). This microgripper was designed in a 'normally open' configuration in which an applied displacement to the input bellows moves the tips of the lateral actuators closer to each other. From the previous section, the free displacement of a single lateral actuator was measured at 33 μm. To ensure reasonable gripping force when the opposing actuators were actuated, the gap between the two actuator tips was designed at 24 μm. As in the extensional actuators, we observed hysteresis in the first cycle of force–displacement data, indicating sticking in the proximal external surfaces during the first actuation cycle. This microgripper is shown gripping a sphere while actuated in Figure 5g.

A separate microgripper system is shown in **Figure 6**. This microgripper was printed in a 'normally closed' configuration in which applied displacement to the input bellows would move the actuator tips away from each other. The benefit of this configuration is that a grip can be maintained even without displacement applied to the input bellows and is similar to the work shown with an actual spider being used as a microgripper in [40]. Similar to the previous system, a 30 μm sphere was printed at the end of a linear extension actuator. This actuator was used to manipulate and apply forces to the sphere with respect to the microgripper (Figure 6a). In Figures 6b,c, we show that the sphere cannot be forced into the microgripper when the gripper is not actuated open; the linear extension actuator buckles as the grippers cannot be forced open. In Figures 6d–g, we show that the normally closed grippers can be opened to capture and grip the sphere. Force is then applied to pull the sphere out of the microgripper by releasing the micro-hydraulic actuator controlling the sphere position. Figure 6g shows the microgripper with no displacement applied to either the microgripper or the linear extension actuator, and the sphere remains captured.

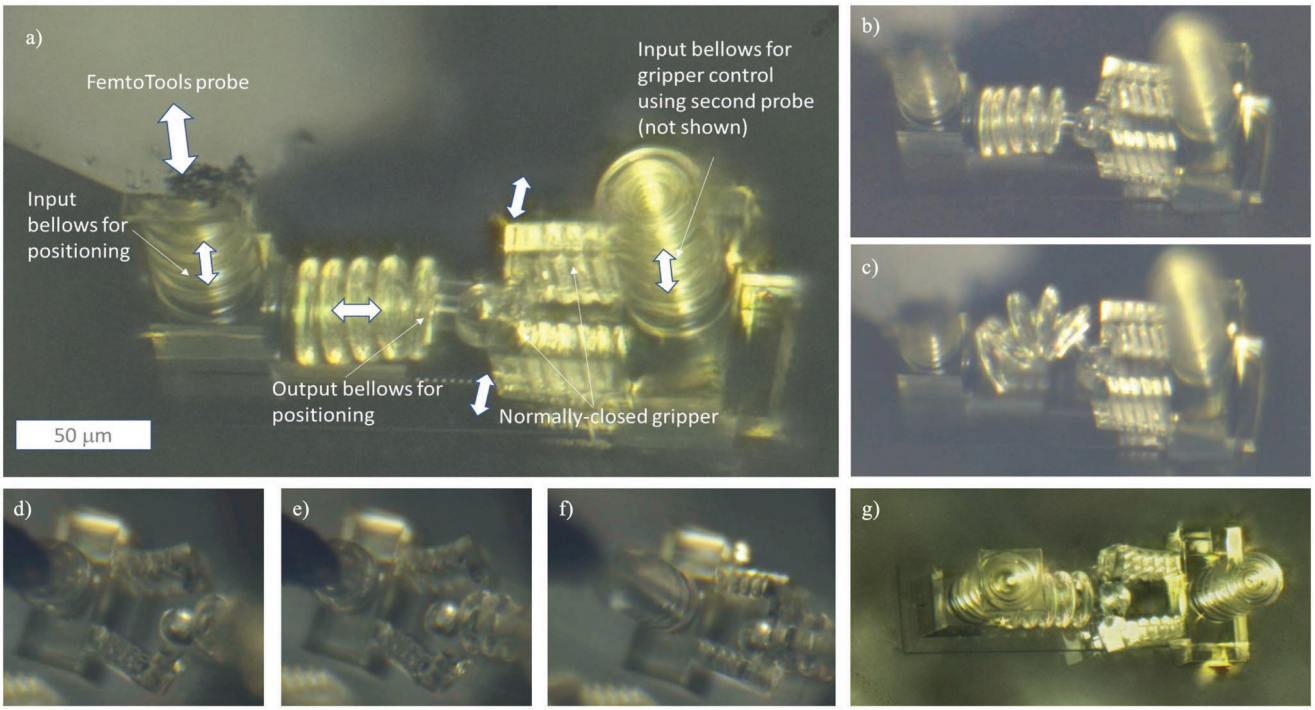

Figure 6. Test results from the normally closed gripper design. a) A microscope image of the microgripper shows the linear actuator printed with a sphere at the end of its output bellows adjacent to (but not inserted into) the normally closed microgripper end effector. b,c) Input displacement is applied to the linear actuator, but due to the normally closed microgripper design, the output bellows of the linear actuator buckles. d–f) A second probe applied an input displacement to the microgripper input bellows while the sphere was actuated into the gripper. The input displacement on the sphere actuator was then released, demonstrating that the microgripper can resist the restoring force from this output bellows. g) A wider view of the captured sphere with zero external input applied to either the linear actuator or the microgripper. A video of this sequence is provided in Supporting Information.

The grip force of this normally closed design can be estimated from the position of the linear actuator controlling the sphere, which was previously characterized in Figure 4d. Assuming that the force at the output bellows is similar to that measured from the input bellows on the return cycle, we estimate that the actuator controlling the sphere position was applying a force on the sphere of approximately 200 – 300 μN given the displacement of 15 – 20 μm. This is very similar to the peak grip force of 350 μN measured from a dead spider when pressurized in [40]. A relatively high estimated grip force, despite the significantly smaller size of the soft robotic microgripper in comparison to the spider, also provides some validation to the scaling analysis described in [40].

Both of these designs demonstrate the feasibility of a 3D soft hydraulic robotic system at only ≈ 150 μm in length scale. While the microgrippers in this work were built from two lateral actuators, three or more opposing lateral actuators could be combined to provide a 3D microgripper. Such a soft robotic system could eventually be used in cellular manipulation or possibly micro-surgery.

2.7. Discussion and Conclusion

This work advances the limits of soft microrobotics by combining the current state of the art in microscale 2PP 3D printing with novel design and fabrication. The feature resolution of 2PP techniques is small enough to allow for compliant geometries from stiff materials more commonly seen in the 2D MEMS community. These small feature sizes allow rigid materials to behave more like soft materials as seen in the imaged lycosid exoskeleton joint. The ability to print in 3D also enables printing fully enclosed fluidic volumes enabling hydraulic actuation without filling or interfacing to another fluid source. We have shown that an uncured resin can act as a viable hydraulic fluid and can actuate in a way inspired by the spider joint exoskeletons imaged as part of this study.

While these results provide an exciting demonstration of microscale hydraulic actuation, the materials used still impose limits on the applications and can be further improved. In particular, the high viscosity of the IP-DIP resin as a hydraulic fluid in the small channels contributes to the hysteresis in the data plots. The specific frequency response was not characterized in this study due to the limited speeds provided by the experimental setup, but bandwidth is expected to be very low. It became apparent that one tradeoff with this actuation approach is the relatively slow operation compared to other MEMS actuators using electrostatic or piezoelectric transduction. Faster and more efficient actuators could be made with a less viscous resin, and we expect that these results can be substantially improved as new resins become available. For example, Nanoscribe's recently released low-modulus resin, IP-PDMS, has a modulus of 15.9 MPa and a much lower viscosity of 2 mPa s, close to the

viscosity of water and very similar to the estimated viscosity of hemolymph, 0.6 – 3.7 mPa s.[60]

In addition, it should be noted that the fabrication process itself has implications beyond hydraulic actuation for soft microrobotics. Capturing printing resin as a hydraulic fluid could be useful in scaling down microfluidic logic as previously demonstrated in [59, 61, 62]. Similarly, this embedded hydraulic fluid can be advantageous toward scaling down recent results on novel soft electrically controlled pumps.[63] In general, electrical transduction methods could be made compatible with this 3D printing process by adding a metallization step as previously demonstrated in [64]. Overall, this work provides a path forward for 3D printed hydraulic microsystems, including microrobotics.

3. Experimental Section

Micro CT Imaging: The internal structure of the spider legs was scanned with the ZEISS Xradia 510 Versa. The leg joints were prepared by staining the spider legs in iodine solution, encasing into Devcon 5 min epoxy and mounting the leg to a 3 mm diameter wooden stick. A video of the micro CT imaging has been included in the Supporting Information.

File Preparation with 2PP: The structures were modeled in Autodesk Inventor and SolidWorks and fabricated using two-photon polymerization (2PP) on a Nanoscribe Photonic Professional 3D printer from a standard STL file common to additive manufacturing (Figure 2). The STL file was prepared in Describe software to interface with the 2PP printer. The printer fabricates a 3D model in slices by laser curing each slice in a 2D plane from a drop of photo-curable resin referred to as IP-DIP by Nanoscribe.

2PP Fabrication: Microfabrication was carried out using a Photonic Professional GT system (Nanoscribe GmbH) using the IP-DIP photoresist. All geometries were patterned on fused silica slides using a 63X objective. Fabrication was performed in the dip-in laser lithography (DiLL) configuration, using galvo-mode with a laser power of 22.5 mW, 10 mm s^{-1} writing speed, and a hatching and slicing distance of 300 nm. Fabricated parts were developed in subsequent Propylene glycol methyl ether acetate (PGMEA) and isopropyl alcohol (IPA) baths for 5 min each to remove uncured resist from the outer surfaces.

Microactuator Characterization: FemtoTools Microforce Sensing Probes were used in combination with the FT-FS1000/FT-RS1000 micromechanical testing systems to apply and measure the forces on the input bellows. The devices were imaged on a Keyence VHX-1000 digital microscope. An uncertainty of 9.9 µN was calculated from the standard deviation of 2000 data points captured from the FemtoTools sensor signal under no load. This includes uncertainty from the sensor itself and any noise from the wiring and interface. A Keyence VHX-1000 microscrope with a 50–500x objective was utilize for its 100 mm working distance. The relative distance measurements were taken from the images using Keyence XY Measurement Software VHX-H1M1 v. 1.0. The uncertainty of the Keyence measurement output was 2 µm at 500x magnification given the test setup and microscope lighting conditions.

Optical Spectrum Characterization: Florescent and incandescent light sources were measured independently with a Spectral Products SM442 Spectrometers with counts over a 400 ms integration time. The sensor manufacturer's stated sensitivity is 160 lx s over a spectral range of 200–1050nm. The specific wavelength of concern for the Nanoscribe IP-DIP resin is 390 nm (the 2PP interaction wavelength). The power density from the incandescent source at 60 cm was calculated to be 13.2 ± 0.4 W m^{-1} at the location of the bellows structure assuming uniform spherically radial power density. For an area of 150 µm × 150 µm, this would result in an absorbed energy of approximately 150 mJ over the full spectrum after the 6 days of testing from the incandescent light source.

Supporting Information

Supporting Information is available from the Wiley Online Library or from the author.

Acknowledgements

The authors would like to acknowledge the support of the Army Research Laboratory for fabrication and testing equipment and resources.

Conflict of Interest

The authors declare no conflict of interest.

Data Availability Statement

The data that support the findings of this study are available from the corresponding author upon reasonable request.

Keywords

bio-inspiration, micro-hydraulics, soft robotics, two-photon polymerization

Received: June 29, 2022
Revised: January 25, 2023
Published online:

[1] T. J. Wallin, J. Pikul, R. F. Shepherd, *Nat. Rev. Mater.* **2018**, *3*, 84.
[2] D. W. Schuldt, J. Rife, B. Trimmer, *Bioinspiration Biomimetics* **2015**, *10*, 016018.
[3] K. J. Quillin, *J. Exp. Biol.* **1999**, *202*, 661.
[4] G. M. Farley, M. J. Wise, J. S. Harrison, G. P. Sutton, C. Kuo, S. N. Patek, *J. Exp. Biol.* **2019**, *222*, jeb201129.
[5] M. Cianchetti, C. Laschi, A. Menciassi, P. Dario, *Nat. Rev. Mater.* **2018**, *3*, 143.
[6] W. Hu, G. Z. Lum, M. Mastrangeli, M. Sitti, *Nature* **2018**, *554*, 81.
[7] S. Kim, C. Laschi, B. Trimmer, *Trends Biotechnol.* **2013**, *31*, 287.
[8] B. J. Nelson, I. K. Kaliakatsos, J. J. Abbott, *Annu. Rev. Biomed. Eng.* **2010**, *12*, 55.
[9] S. Palagi, P. Fischer, *Nat. Rev. Mater.* **2018**, *3*, 113.
[10] L. Ricotti, *Sci. Rob.* **2017**, *2*, eaaq0495.
[11] M. Sitti, *Proc. IEEE* **2015**, *103*, 205.
[12] S. Fusco, M. S. Sakar, S. Kennedy, C. Peters, R. Bottani, F. Starsich, A. Mao, G. A. Sotiriou, S. Pané, S. E. Pratsinis, D. Mooney, B. J. Nelson, *Adv. Mater.* **2014**, *26*, 952.
[13] A. P. Gerratt, S. Bergbreiter, *Sens. Actuators, A* **2012**, *177*, 16.
[14] M. Soreni-Harari, R. St. Pierre, C. McCue, K. Moreno, S. Bergbreiter, *Soft Rob.* **2020**, *7*, 59.
[15] J. Paek, I. Cho, J. Kim, *Nat. Sci. Rep.* **2015**, *5*, 10768.
[16] J. Shintake, V. Cacucciolo, D. Floreano, H. Shea, *Adv. Mater.* **2018**, *30*, 1707035.
[17] M. D. Volder, D. Reynaerts, *J. Micromech. Microeng.* **2010**, *20*, 043001.
[18] E. Milana, B. Gorissen, E. De Borre, F. Ceyssens, D. Reynaerts, M. De Volder, *Soft Rob.* **2023**, *10*, 197.
[19] J.-S. Plante, S. Dubowsky, *Smart Mater. Struct.* **2007**, *16*, S227.
[20] A. T. Alsharhan, R. Acevedo, R. Warren, R. D. Sochol, *Lab Chip* **2019**, *19*, 2799.

[21] S. Kim, E. Hawkes, K. Choy, M. Joldaz, J. Foleyz, R. Wood, *Proc. IEEE/RSJ Int. Conf. on Intelligent Robots and Systems* **2009**, *2009*, 2228.
[22] Z. Ren, M. Zarepoor, X. Huang, A. P. Sabelhaus, C. Majidi, *Front. Rob. AI* **2021**, *8*, 9.
[23] R. MacCurdy, R. Katzschmann, Y. Kim, D. Rus, in *IEEE Int. Conf. Rob. Autom. (ICRA)*, IEEE, **2016**.
[24] P. Rothemund, S. Kirkman, C. Keplinger, *Proc. Natl. Acad. Sci.* **2020**, *117*, 16207.
[25] J. I. Lipton, S. Angle, R. E. Banai, E. Peretz, H. Lipson, *Adv. Eng. Mater.* **2016**, *18*, 1710.
[26] L. Hines, K. Petersen, G. Z. Lum, M. Sitti, *Adv. Mater.* **2017**, *29*, 1603483.
[27] S. Rosset, H. R. Shea, *Appl. Phys. Rev.* **2016**, *3*, 031105.
[28] H. Zeng, P. Wasylczyk, C. Parmeggiani, D. Martella, M. Burresi, D. S. Wiersma, *Adv. Mater.* **2015**, *27*, 3883.
[29] D. Martella, S. Nocentini, D. Nuzhdin, C. Parmeggiani, D. S. Wiersma, *Adv. Mater.* **2017**, *29*, 1704047.
[30] S. Baghbani Kordmahale, J. Qu, A. Muliana, J. Kameoka, *Sci. Rep.* **2022**, *12*, 21403.
[31] M. Power, A. J. Thompson, S. Anastasova, G.-Z. Yang, *Small* **2018**, *14*, 1703964.
[32] T. Weihmann, M. Gunther, R. Blickhan, *J. Exp. Biol.* **2012**, *215*, 578.
[33] D. Parry, R. H. J. Brown, *J. Exp. Biol.* **1959**, *36*, 654.
[34] C. H. Ellis, *Biol. Bull* **1944**, *86*, 41.
[35] W. F. Whitehead, J. G. Rempel, *Can. J. Zool.* **1959**, *37*, 831.
[36] J. F. Anderson, K. N. Prestwich, *Z. Morph. Tiere* **1975**, *81*, 257.
[37] N. Kellaris, P. Rothemund, Y. Zeng, S. K. Mitchell, G. M. Smith, K. Jayaram, C. Keplinger, *Adv. Sci.* **2021**, *8*, 2100916.
[38] C. Göttler, K. Elflein, R. Siegwart, M. Sitti, *Adv. Sci.* **2021**, *8*, 2003890.
[39] D. Han, H. Gu, J. wan Kim, S. Yokota, *Sens. Actuators, A* **2017**, *257*, 47.
[40] T. F. Yap, Z. Liu, A. Rajappan, T. J. Shimokusu, D. J. Preston, *Adv. Sci.* **2022**, *9*, 2201174.
[41] Y. Politi, L. Bertinetti, P. Fratzl, F. G. Barth, *Philos. Trans. R. Soc., A* **2021**, *379*, 20200332.
[42] V. Chan, J. H. Jeong, P. Bajaj, M. Collens, T. Saif, H. Kong, R. Bashir, *Lab Chip* **2012**, *12*, 88.
[43] J. Odent, T. J. Wallin, W. Pan, K. Kruemplestaedter, R. F. Shepherd, E. P. Giannelis, *Adv. Funct. Mater.* **2017**, *27*, 1701807.
[44] A. Miriyev, K. Stack, H. Lipson, *Nat. Commun.* **2017**, *8*, 596.
[45] J. Morrow, S. Hemleben, Y. Mengüç, *IEEE Rob. Autom. Lett.* **2017**, *2*, 277.
[46] S. E. Bakarich, R. Gorkin, R. Gately, S. Naficy, M. in het Panhuis, G. M. Spinks, *Addit. Manuf.* **2017**, *14*, 24.
[47] S. E. Bakarich, M. i. h. Panhuis, S. Beirne, G. G. Wallace, G. M. Spinks, *J. Mater. Chem. B* **2013**, *1*, 4939.
[48] D. K. Patel, A. H. Sakhaei, M. Layani, B. Zhang, Q. Ge, S. Magdassi, *Adv. Mater.* **2017**, *29*, 1606000.
[49] J. Plott, A. Shih, *Addit. Manuf.* **2017**, *17*.
[50] B. N. Peele, T. J. Wallin, H. Zhao, R. F. Shepherd, *Bioinspir. Biomim.* **2015**, *10*, 055003.
[51] Z. Yu, D. Lau, *J. Mater. Sci.* **2015**, *50*, 7149.
[52] M. M. Sadeghi, H. S. Kim, R. L. B. Peterson, K. Najafi, *J. Microelectromech. Syst.* **2016**, *25*, 557.
[53] A.-I. Bunea, N. del Castillo Iniesta, A. Droumpali, A. E. Wetzel, E. Engay, R. Taboryski, *Micro* **2021**, *1*, 164.
[54] S. Schweiger, T. Schulze, S. Schlipf, P. Reinig, H. Schenk, *J. Opt. Microsyst.* **2022**, *2*, 033501.
[55] J. Bauer, A. Guell Izard, Y. Zhang, T. Baldacchini, L. Valdevit, *Adv. Mater. Technol.* **2019**, *4*, 1900146.
[56] L. R. Meza, A. J. Zelhofer, N. Clarke, A. J. Mateos, D. M. Kochmann, J. R. Greer, *Proc. Natl. Acad. Sci.* **2015**, *112*, 11502.
[57] Nanoscribe, *Material Safety Data Sheet IP-DIP Photoresist*, **2017**, Rev. EN01/2017.
[58] F. Ilievski, A. D. Mazzeo, R. F. Shepherd, X. Chen, G. M. Whitesides, *Angew. Chem.* **2011**, *123*, 1930.
[59] J. D. Hubbard, R. Acevedo, K. M. Edwards, A. T. Alsharhan, Z. Wen, J. Landry, K. Wang, S. Schaffer, R. D. Sochol, *Sci. Adv.* **2021**, *7*, eabe5257.
[60] C. Göttler, G. Amador, T. van de Kamp, M. Zuber, L. Böhler, R. Siegwart, M. Sitti, *Soft Matter* **2021**, *17*, 5532.
[61] P. N. Duncan, T. V. Nguyen, E. E. Hui, *Proc. Natl. Acad. Sci.* **2013**, *110*, 18104.
[62] M. Wehner, R. L. Truby, D. J. Fitzgerald, B. Mosadegh, G. M. Whitesides, J. A. Lewis, R. J. Wood, *Nature* **2016**, *536*, 451.
[63] V. Cacucciolo, J. Shintake, Y. Kuwajima, S. Maeda, D. Floreano, H. Shea, *Nature* **2019**, *572*, 516.
[64] S. Kim, C. Velez, R. S. Pierre, G. L. Smith, S. Bergbreiter, *J. Microelectromech. Syst.* **2020**, *29*, 544.